ELSEVIER

Journal of Crystal Growth 149 (1995) 253–265

JOURNAL OF CRYSTAL GROWTH

Shear stabilization of morphological instability during directional solidification

T.P. Schulze, S.H. Davis *

Department of Engineering Sciences and Applied Mathematics, Northwestern University, Evanston, Illinois 60208, USA

Received 9 August 1994; manuscript received in final form 15 December 1994

Abstract

A linear stability analysis is performed on the interface formed during the directional solidification of a dilute binary alloy in the presence of a time-periodic flow. In general, the flow is generated by translating the crystal relative to the far-field flow in elliptical orbits parallel to the interface. The presence of this complex, unsteady flow can either stabilize or destabilize the system relative to the case without flow, with the result depending on the frequency and amplitude of the oscillations as well as the properties of the material. We find, however, that proper selection of the frequency and amplitude of the modulation, both physically realizable, can eliminate the possibility of morphological instability for a significant range of solute concentrations.

1. Introduction

The manufacturing of single crystals with uniform material properties is frequently hampered by the presence of morphological instabilities during the solidification of multi-component materials. These nonuniformities result from an interaction between surface morphology and the concentration gradients created by solute rejection. In order to eliminate these nonuniformities, it is necessary to suppress the instability. In the context of directional solidification, this can be done by producing materials with sufficiently low solute concentrations, or by reducing the pulling speed of the solidification front [1].

When it is undesirable to operate within this restricted range of parameters, some other method of stabilization is necessary. In the 1960's, Hurle suggested that flow in the melt, either forced or resulting from natural convection, might be used to stabilize the interface. Since then, a number of studies have investigated the effect of various flows on morphological stability. Delves [2], Coriell et al. [3], Forth and Wheeler [4] and Hobbs and Metzener [5] have all studied the influence of parallel flows on morphological instability. A general result for this type of flow is that disturbances with wavevectors parallel to the cross-stream direction will be unaffected by the flow; thus, when stabilizing, a parallel flow selects a cellular pattern that is periodic in the cross-stream direction. Brattkus and Davis [6,7], McFadden et al. [8] and Merchant and Davis [9] have studied the influence of various nonparallel flows. For a brief review of studies involving the interaction of a solidifying interface and a forced

* Corresponding author.

SSDI 0022-0248(94)00832-9

flow see Schulze and Davis [10], where a list of more extensive reviews covering the role of convection in solidification may also be found.

This paper follows up on the work of Schulze and Davis [10], who studied the influence of steady and oscillatory shears on interfacial stability during directional solidification. They found that the purely oscillatory motion of the crystal parallel to the interface – resulting in solidification into a compressed Stokes layer (CSL) – provided stabilization for two-dimensional disturbances of arbitrary wavelength in the limit of small oscillation amplitude, provided the frequency of the oscillations is within a calculated range. The amount of stabilization obtained is proportional to the square of the modulation amplitude. The CSL is generated by oscillating the crystal back and forth parallel to the interface during directional solidification. The compression of the Stokes layer is the result of flow normal to the boundary. Note that, like the parallel flows mentioned above, stabilization can only be achieved in two dimensions with the CSL.

Motivated by the work of Kelly and Hu [11] on Bénard convection, we attempt to extend the stabilizing influence of the CSL to three dimensions by considering the influence of nonplanar oscillations. Specifically, we consider the effect of adding a second oscillation of the same frequency perpendicular to the first; the two forcings may differ in amplitude and phase. This corresponds to translating the crystal relative to the far-field flow in elliptical orbits parallel to the interface, generating a complex, unsteady flow. The essence of this idea was also suggested by Delves [2], who wrote in his paper on solidification into a Blasius boundary layer, "it might be possible to ensure complete stability of the interface by rapid and continuous changes in the flow pattern".

When Kelly and Hu applied this same type of forcing to one or both of the horizontal boundaries in three-dimensional Bénard convection, they found that convection is delayed, provided the two oscillations are not perfectly in or out of phase. By taking the amplitude of the oscillations to be large, they found that the amount of stabilization could be substantial. In an effort to obtain more significant stabilization here, we investigate the effect of large amplitude oscillations on morphological instability.

We begin in the next section with the governing equations and boundary conditions. In Section 3 we review the weakly-forced CSL results and extend them for the case of nonplanar oscillations. In Section 4 we consider the response to strongly forced oscillations, and in Section 5 we briefly discuss the absence of subharmonic instability in this system. In Section 6 we discuss the stability of the related hydrodynamic system. In Section 7, we summarize and conclude.

2. Governing equations

We consider the directional solidification of a dilute binary mixture at constant speed V. We choose a coordinate system with x and y-axis located at the mean position of the crystal interface, moving with the front. The equations governing the system in the fluid region are the Navier–Stokes, continuity, and solute diffusion equations. To simplify the analysis, we neglect latent heat and density changes, and we assume equal densities and thermal properties between the two phases. We also assume that heat diffuses much faster than solute, and, in this limit, the temperature field is fixed and depends linearly on the vertical coordinate (frozen temperature approximation [12]). In nondimensional form, these equations are

$$\Omega \boldsymbol{u}_t + \epsilon \boldsymbol{u} \cdot \nabla \boldsymbol{u} - \boldsymbol{u}_z = -\nabla p + S\nabla^2 \boldsymbol{u}, \tag{2.1a}$$

$$\nabla \cdot \boldsymbol{u} = 0, \tag{2.1b}$$

$$\Omega C_t + \epsilon \boldsymbol{u} \cdot \nabla C - C_z = \nabla^2 C, \tag{2.1c}$$

$$T = z. \tag{2.1d}$$

We have nondimensionalized the equations using the following scalings:

$$\boldsymbol{x} \to (D/V)\boldsymbol{x}, \quad \boldsymbol{u} \to U\boldsymbol{u}, \quad t \to t/\omega, \tag{2.2a}$$

$$p \to \rho UVp, \quad T \to (GD/V)T + T_0,$$

$$C \to (C_\infty - C_\infty/k)C + C_\infty/k, \tag{2.2b}$$

where D is the solute diffusivity, V is the crystal pulling speed, U is the amplitude of the velocity oscillations, ρ is the material density, C_∞ is the

far field concentration, ω is the angular frequency of the elliptical oscillations of the crystal, G is the thermal gradient, T_0 is the temperature of the interface in the basic state, and k is the segregation coefficient.

The nondimensional parameters that appear in the equations and boundary conditions are the morphological number M, the surface energy parameter Γ, the Schmidt number S, the nondimensional angular frequency Ω, the segregation coefficient k, and a parameter ϵ measuring the amplitude of the lateral oscillations in units of pulling speed:

$$M = mVC_\infty(1 - 1/k)/GD, \tag{2.3a}$$

$$\Gamma = T_m\gamma V/DL_V mC_\infty(1 - 1/k), \tag{2.3b}$$

$$S = \nu/D, \tag{2.3c}$$

$$\Omega = \omega D/V^2, \tag{2.3d}$$

$$\epsilon = U/V. \tag{2.3e}$$

The far-field boundary conditions are, as $z \to \infty$,

$$u \to 0, \tag{2.4a}$$

$$v \to 0, \tag{2.4b}$$

$$w \to 0, \tag{2.4c}$$

$$C \to 1, \tag{2.4d}$$

and the interfacial conditions, evaluated at the interface $z = h(x, y, t)$, are

$$u = \cos t, \tag{2.5a}$$

$$v = \beta \cos(t - \gamma), \tag{2.5b}$$

$$w = 0, \tag{2.5c}$$

$$C = M^{-1}h - 2\Gamma H, \tag{2.5d}$$

$$\left[1 + \Omega h_t + \epsilon \cos(t)h_x + \epsilon\beta \cos(t - \gamma)h_y\right] \times \left[1 + (k - 1)C\right] = C_z - C_x h_x - C_y h_y, \tag{2.5e}$$

where β is the ratio of the amplitudes of the two perpendicular oscillations and γ is the phase difference between them. The mean curvature of the interface, H, is given by

$$2H = \nabla \cdot \left[\nabla h\left(1 + |\nabla h|^2\right)^{-1/2}\right]. \tag{2.6}$$

Notice that this problem may also be treated by switching to a frame of reference where the crystal is stationary, and the fluid oscillates. In this approach, the boundary condition (2.5e) reduces to the usual one for solidification without flow, and the Navier–Stokes equations have a time-periodic forcing term generated by the non-Galilean transformation.

The basic state for this system takes the form

$$\bar{u} = e^{-Bz} \cos(t - Az), \tag{2.7a}$$

$$\bar{v} = \beta e^{-Bz} \cos(t - Az - \gamma), \tag{2.7b}$$

$$\bar{w} = 0, \tag{2.7c}$$

$$\bar{C} = 1 - e^{-z}, \tag{2.7d}$$

$$\bar{h} = 0, \tag{2.7e}$$

where A and B are constants given in the Appendix.

To analyse the response of this state to infinitesimal perturbations, we disturb each of these quantities, and separate the disturbances into normal modes:

$$u = \bar{u} + \left[\hat{u}(z, t)\, e^{i(\alpha_1 x + \alpha_2 y)}\, e^{\sigma t} + \text{c.c.}\right], \tag{2.8a}$$

$$v = \bar{v} + \left[\hat{v}(z, t)\, e^{i(\alpha_1 x + \alpha_2 y)}\, e^{\sigma t} + \text{c.c.}\right], \tag{2.8b}$$

$$w = \hat{w}(z, t)\, e^{i(\alpha_1 x + \alpha_2 y)}\, e^{\sigma t} + \text{c.c.}, \tag{2.8c}$$

$$C = \bar{C} + \hat{C}(z, t)\, e^{i(\alpha_1 x + \alpha_2 y)}\, e^{\sigma t} + \text{c.c.}, \tag{2.8d}$$

$$h = \hat{h}(t)\, e^{i(\alpha_1 x + \alpha_2 y)}\, e^{\sigma t} + \text{c.c.} \tag{2.8e}$$

Here we are seeking time-periodic eigenfunctions with the same period as the basic state, and σ is the Floquet exponent. If the real part of σ is not zero, then the disturbances will experience a net growth or decay over one period.

By taking the curl of the Navier–Stokes equations twice, and using the continuity equation to simplify the result, we arrive at a fourth-order disturbance equation for the vertical component of the disturbance velocity. Combining this with the disturbance equation for the solute field we have a sixth-order boundary-value problem. Because the shape of the interface is also undetermined, we require an additional interfacial condition, giving us a total of seven boundary conditions.

In the fluid we have

$$(D^2 + D - \alpha^2 - \Omega\partial_t)\hat{C} = \epsilon\left(i\alpha_1\bar{u}\hat{C} + i\alpha_2\bar{v}\hat{C} + e^{-z}\hat{w}\right) + \Omega\sigma\hat{C}, \quad (2.9a)$$

$$(D^2 - \alpha^2)\left[S(D^2 - \alpha^2) + D - \Omega\partial_t\right]\hat{w} = \epsilon\left[i\alpha_1\bar{u}(D^2 - \alpha^2)\hat{w} - i\alpha_1\hat{w}D^2\bar{u} + i\alpha_2\bar{v}(D^2 - \alpha^2)\hat{w} - i\alpha_2\hat{w}D^2\bar{v}\right] + \Omega\sigma(D^2 - \alpha^2)\hat{w}, \quad (2.9b)$$

where D indicates $\partial/\partial z$, ∂_t indicates $\partial/\partial t$ and $\alpha^2 = \alpha_1^2 + \alpha_2^2$.

In the far field we have, as $z \to \infty$,

$$\hat{C}(z, t) \to 0, \quad (2.10a)$$

$$\hat{w}(z, t) \to 0, \quad (2.10b)$$

$$D\hat{w}(z, t) \to 0. \quad (2.10c)$$

The interfacial conditions, transferred to $z = 0$, are

$$\hat{h} = \frac{1}{M^{-1} + \alpha^2\Gamma - 1}\hat{C} \equiv \lambda\hat{C}, \quad (2.11a)$$

$$D\hat{C} = \left\{k - 1 + \lambda\left[k + \Omega\partial_t + i\epsilon\alpha_1 \cos t + i\epsilon\alpha_2\beta \cos(t - \gamma)\right]\right\}\hat{C}, \quad (2.11b)$$

$$\hat{w} = 0, \quad (2.11c)$$

$$D\hat{w} = \lambda\left[i\alpha_1\hat{C}D\bar{u} + i\alpha_2\hat{C}D\bar{v}\right]. \quad (2.11d)$$

3. Small amplitude forcing

In this section we shall seek conditions on the morphological number M such that the system is neutrally stable in the limit of small forcing, $\epsilon \to 0$. In this limit, we find that $\sigma = 0$ on the neutral curve, and expanding the reciprocal of the morphological number as

$$M^{-1} = M_0 + \epsilon^2 M_2 + \ldots, \quad (3.1)$$

we get

$$M_2 = \left[(\cos\theta + \beta\cos\gamma\sin\theta)^2 + \beta^2\sin^2\theta\sin^2\gamma\right]M_2^{(2D)}, \quad (3.2)$$

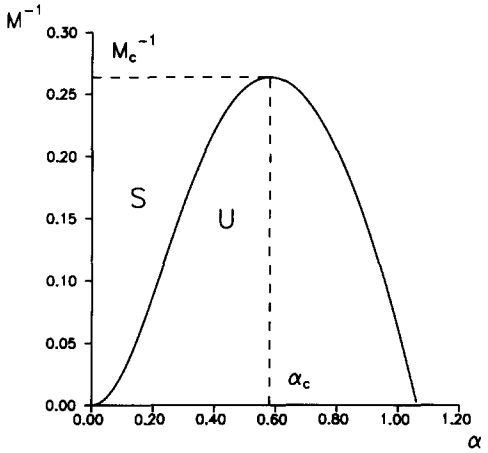

Fig. 1. Directional solidification without flow. $M^{-1} \equiv M_0$ versus α for $S = 81.0$, $k = 0.3$ and $\Gamma = 0.6$. The region above the curve corresponds to a stable (S) interface, and the region below the curve corresponds to an unstable (U) interface.

where $M_2^{(2D)}$ is the two-dimensional result for the CSL, β is the amplitude ratio, γ is the phase difference between the oscillations, and $\theta = \tan^{-1}(\alpha_2/\alpha_1)$ is the angle that the disturbance wave vector makes with the x-axis. The coefficient in Eq. (3.2) takes the same form as that found by Kelly and Hu [11] when they applied the same type of forcing to the Bénard problem.

In Fig. 1 we present a typical neutral curve for the leading-order (no flow) result. Recall that M_0 is the reciprocal of M when there is no flow. For a given wavenumber α, if M_0 is above (below) this curve, disturbances with that wavenumber will decay (grow). For the no-flow system to be linearly stable, M_0 must be above this curve for all wavenumbers. As one decreases M_0, the instability will set in at the a critical wavelength, α_c. This result is the same in two and three dimensions. In three dimensions, α refers to the magnitude of the wavevector, $(\alpha_1^2 + \alpha_2^2)^{1/2}$.

In Fig. 2 we show a typical map of the regions in the α–Ω plane where the CSL stabilizes ($M_2^{(2D)} < 0$) and destabilizes ($M_2^{(2D)} > 0$) the interface in two dimensions [10]. Notice that there is a range of forcing frequencies for which disturbances of arbitrary wavenumber can be stabilized. We refer to this as the *window of stabilization*. It is important to be able to stabilize arbitrary wave-

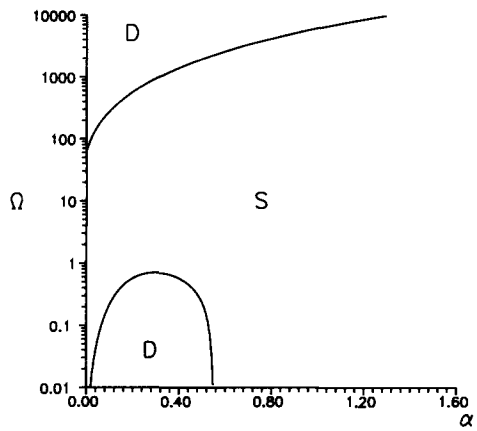

Fig. 2. Directional solidification into CSL. Regions of the $\alpha-\Omega$ plane where the flow stabilizes (S) or destabilizes (D) the interface relative to the case without flow. $S = 81.0$ and $k = 0.3$; results are independent of Γ.

lengths because the critical wavelength depends on various parameters and varies widely. Also, unless $M_2^{(2D)} < 0$ for all wavenumbers, forcing with a sufficiently large amplitude may cause wavenumbers other than α_c to become unstable.

In three dimensions, we see from (3.2) that for oscillations that are either perfectly in or out of phase (corresponding to a phase angle that is an integral multiple of π), there will be some θ_c for which the correction to the no-flow result, M_2, is zero. This means that the flow will be able to destabilize the interface if $M_2^{(2D)} > 0$, but acts only as a pattern selection mechanism if $M_2^{(2D)} < 0$, with disturbances oriented at the angle θ_c being the least stable. This is a degenerate case corresponding to a single oscillation along an axis lying in the x–y plane. The result is therefore equivalent to that for the CSL in three dimensions.

When the phase between the oscillations, γ, is not a multiple of π, the factor appearing in front of $M_2^{(2D)}$ is positive, and it is possible to stabilize an arbitrary three-dimensional disturbance provided $M_2^{(2D)} < 0$. Thus the ability of the nonplanar oscillations to stabilize the interface is predicted by the results for the CSL, and the window of stabilization is the same for both cases.

It is easy to show that the maximum stabilization occurs when the phase angle is $\pi/2$, with the stabilization being greater along whichever axis has the largest amplitude oscillations. If the amplitude ratio, β, is one, there will be no preferred direction for cell orientation.

4. Finite amplitude forcing

In the previous section we showed that some degree of stabilization can be achieved by using small amplitude, nonplanar oscillations with a frequency lying within a given range. In this section we show that in many cases the Mullins and Sekerka interfacial mode can be entirely suppressed if these oscillations have sufficiently large amplitude.

4.1. Method of solution

These calculations were done using the same technique used by Hall [13] in studying the hydrodynamic stability of a Stokes layer. We begin by assuming a Fourier expansion for each of the dependent variables:

$$\hat{C} = \sum_{m=-\infty}^{\infty} C_m(z)\, e^{imt}, \tag{4.1a}$$

$$\hat{w} = \sum_{m=-\infty}^{\infty} w_m(z)\, e^{imt}. \tag{4.1b}$$

The position of the interface, h, has been eliminated from the analysis via substitution.

The two partial differential equations that govern the system are converted into an infinite system of coupled ordinary differential equations of the form

$$\begin{aligned}[\mathrm{D}^2-\alpha^2]\big[S(\mathrm{D}^2-\alpha^2)+\mathrm{D}-\sigma\Omega-\mathrm{i}m\Omega\big]w_m &= \tfrac{1}{2}\mathrm{i}\epsilon\big[\chi\, e^{-rz}(\mathrm{D}^2-\alpha^2-r^2)w_{m-1} \\ &\quad +\bar{\chi}\, e^{-\bar{r}z}(\mathrm{D}^2-\alpha^2-\bar{r}^2)w_{m+1}\big],\end{aligned} \tag{4.2a}$$

$$\begin{aligned}[\mathrm{D}^2-\alpha^2+\mathrm{D}-\sigma\Omega-\mathrm{i}m\Omega]C_m &= \tfrac{1}{2}\mathrm{i}\epsilon\big[\chi\, e^{-rz}C_{m-1}+\bar{\chi}\, e^{-\bar{r}z}C_{m+1}\big] \\ &\quad +\epsilon e^{-z}w_m,\end{aligned} \tag{4.2b}$$

for each integer m. Here, $\chi = \alpha_1 + \alpha_2\beta\, e^{-i\gamma}$ and $r = B + iA$. The bars over these quantities indicate their complex conjugates.

Notice that the equations for the w_m are not coupled to the equations for the C_m. Thus, the flow-field solution is essentially the same as for the Stokes layer. If we neglect the right-hand side of Eq. (4.2a), we find a solution

$$w_m^* = a_m\, e^{-\alpha z} + b_m\, e^{-\nu_m z}, \tag{4.3}$$

for each m, where

$$\nu_m = \left[1 + \sqrt{1 + 4S(S\alpha^2 + \sigma\Omega + im\Omega)}\,\right]/2S. \tag{4.4}$$

The a_m and b_m are arbitrary coefficients that are determined, up to a multiplicative constant, by application of the interfacial conditions. We have already used the far-field condition to eliminate the unbounded solutions.

Now, if we add to this solution terms generated by the right-hand side of the equation, we find that the solutions w_{m-1}^* and w_{m+1}^* each generate a term in the solution for w_m. Similarly, each of the terms in the complete solutions for w_{m+1} and w_{m-1} will ultimately produce terms in the solution for w_m. This produces an infinite cascade of terms for each of the Fourier components that are related to one another in a Pascal-triangle-like structure where a given term is related to two of its predecessors by a recursion relation.

To find these recursion relations, we observe that each term in the solution for w_m is of the form

$$w_{nmj} = a_n p_{nmj}\, e^{-[\alpha + jB - i(n-m)A]z} + b_n q_{nmj}\, e^{-[\nu_n + jB - i(n-m)A]z}, \tag{4.5}$$

where n is an integer and j is a nonnegative integer. Substituting this anzatz into Eq. (4.2a) results in the recursion relations for the coefficients p_{nmj} and q_{nmj} given in the Appendix.

The general solution for each w_m then takes the form

$$w_m = \sum_{n=-\infty}^{\infty} \sum_{j=0}^{\infty} a_n p_{nmj}\, e^{-[\alpha + jB - i(n-m)A]z} + b_n q_{nmj}\, e^{-[\nu_n + jB - i(n-m)A]z}. \tag{4.6}$$

Similarly, one can generate a solution for each C_m:

$$C_m = \sum_{n=-\infty}^{\infty} \sum_{j=0}^{\infty} a_n \tilde{p}_{nmj}\, e^{-[\alpha + jB - i(n-m)A + 1]z} + b_n \tilde{q}_{nmj}\, e^{-[\nu_n + jB - i(n-m)A + 1]z} + d_n r_{nmj}\, e^{-[\rho_n + jB - i(n-m)A]z}, \tag{4.7}$$

where

$$\rho_n = \left[1 + \sqrt{1 + 4(\alpha^2 + \sigma\Omega + im\Omega)}\,\right]/2, \tag{4.8}$$

and the d_n are more arbitrary coefficients to be determined by application of the interfacial conditions. Because the solute equation is coupled to the velocity equation, the coefficients $\tilde{p}_{nmj}$ and $\tilde{q}_{nmj}$ depend on p_{nmj} and q_{nmj}, respectively. These recursion relations, along with those for the r_{nmj}, are given in the Appendix.

With these solutions in hand, one can then apply the interfacial conditions which take the form

$$w_m = 0, \tag{4.9a}$$

$$Dw_m = -\tfrac{1}{2}i\lambda\left(\chi r C_{m-1} + \bar{\chi}\bar{r} C_{m+1}\right), \tag{4.9b}$$

$$DC_m = [k - 1 + \lambda(k + im\Omega + \sigma\Omega)]C_m + \tfrac{1}{2}i\epsilon\lambda\left(\chi C_{m-1} + \bar{\chi} C_{m+1}\right). \tag{4.9c}$$

This results in an infinite sequence of coupled homogeneous equations for the coefficients a_n, b_n and d_n.

If we truncate our solution so that m and n run from $-N$ to N, we generate a linear system with a $6N + 3$ by $6N + 3$ coefficient matrix. Each component of this matrix is a sum over the index j, which runs from zero to, say, N. With all of the physical parameters fixed, we then evaluate the determinant iteratively in order to locate the eigenvalues, or Floquet exponents, σ.

In general, the number of modes N required for this method to converge increases with both ϵ and α. For a value of $\epsilon = 20$, $N = 15$ is sufficient for resolving the neutral curve, but for a value of $\epsilon = 60$ a value of $N = 30$ is necessary. We were unable to perform calculations with $N > 35$ due to a lack of computer memory. Finally, notice that no truncation of the vertical domain is neces-

sary with this method – the far field boundary conditions are satisfied exactly.

4.2. Results

Our primary objective in this section is to demonstrate that the morphological instability in the absence of flow can be suppressed by using sufficiently strong oscillations of the crystal. For demonstration purposes we use material parameters characteristic of a lead–tin alloy, unless indicated otherwise. These parameter values are presented in Table 1 along with those for silicon–tin and succinonitrile–acetone (SCN–Ace).

Guided by the results for weak oscillations, we choose the value $\Omega = 10$ for the nondimensional forcing frequency. This lies within the window of stabilization found previously and is close to the optimal frequency for stabilization purposes. This can be seen by examining Fig. 3 where we plot M_2 versus Ω with $\alpha = \alpha_c$, the critical value for the no-flow case.

In Fig. 4 we plot M^{-1} versus α for speed ratios $\epsilon = \{0, 20, 40, 60\}$. Recall that when $\epsilon = 0$ we recover the no-flow results of Mullins and Sekerka as shown in Fig. 1. Notice that for $\epsilon = 60$ the neutral curve lies entirely beneath the horizontal axis, indicating that the instability has been eliminated for all physically realizable morphological numbers. Also notice that as the neutral curve drops below the horizontal axis there is an abrupt shift in the critical wavenumber from a finite value to zero.

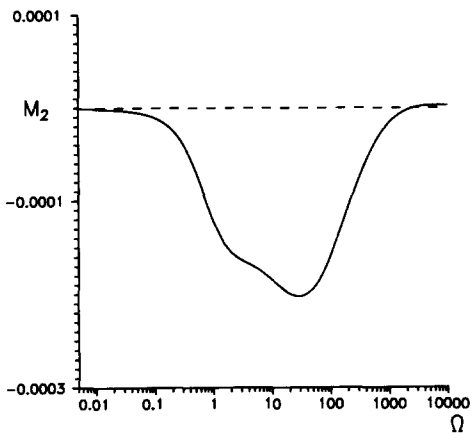

Fig. 3. Directional solidification into CSL. M_2 as a function of Ω with $\alpha = \alpha_c$, the critical value for the no-flow case. $k = 0.3$ and $S = 81.0$. Notice that the maximum stabilization occurs for $\Omega \approx 10$.

These calculations were done for the two-dimensional case (CSL). We have verified that the instability may be entirely suppressed in three-dimensions by using an amplitude ratio $\beta = 1$ and a phase difference of $\pi/2$. In this case the suppression of disturbances is independent of their orientation θ, and the dependence on wavenumber is identical to that of the two-dimensional case.

If we continue to increase ϵ past the value necessary to stabilize the interface, we find, for these material parameters and operating conditions, that the stabilization trend is reversed. This is demonstrated in Fig. 5 where we plot M^{-1} versus ϵ with $\alpha = \alpha_c$, the critical value in the

Table 1
Parameter values used in the calculations (unless otherwise indicated).

Parameter	Symbol	Pb–Sn	Si–Sn	SCN–Ace	Units
Kinematic viscosity	ν	2.43×10^{-3}	0.3	2.6×10^{-2}	cm^2/s
Solute diffusivity	D	3.0×10^{-5}	2.5×10^{-4}	1.3×10^{-5}	cm^2/s
Liquidus slope	m	−2.33	−4.6	−3.04	K/wt%
Melting point	T_m	600.6	1687	331.2	K
Surface free energy	γ	42.6	373	8.95	erg/cm^2
Latent heat/unit volume	L_V	2.56×10^9	4.19×10^{10}	4.64×10^5	erg/cm^3
Temperature gradient	G	200.0	200.0	10.0	K/cm
Segregation coefficient	k	0.3	0.016	0.1	–
Schmidt number	S	81.0	1200	2050	–
Surface energy parameter	Γ	0.61	2.1×10^{-3}	1.84	–

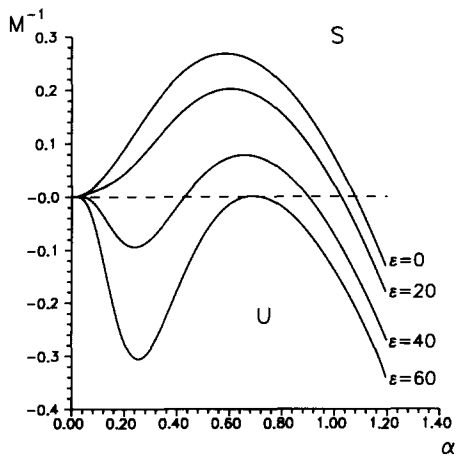

Fig. 4. Directional solidification into CSL. Plot of M^{-1} as a function of α for $k = 0.3$, $S = 81.0$, $\Gamma = 0.6$, $\Omega = 10.0$ and $\epsilon = \{0, 20, 40, 60\}$. The region above each curve corresponds to a linearly stable (S) interface, and the region below each curve corresponds to a linearly unstable (U) interface. As ϵ increases the critical value of M^{-1} decreases. Notice that for $\epsilon \approx 60$ the interface is absolutely stable.

absence of flow. This may indicate that there is an amplitude window as well as a frequency window for stabilization. Calculations for larger values of ϵ were not made due to the increasing difficulty of performing these computations which

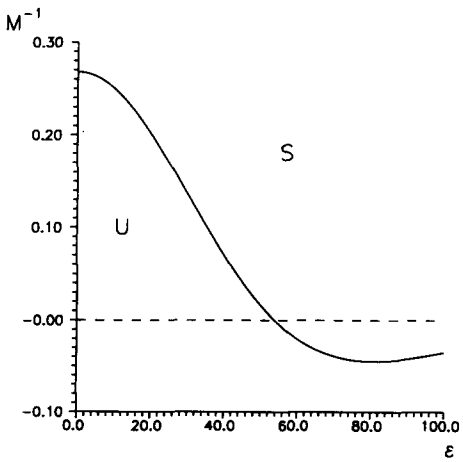

Fig. 5. Directional solidification into CSL. Plot of M^{-1} versus ϵ with $\alpha = \alpha_c$, the critical value for the no-flow case. $k = 0.3$, $S = 81.0$ and $\Omega = 10.0$. This plot shows that the stabilizing trend eventually reverses as ϵ is increased.

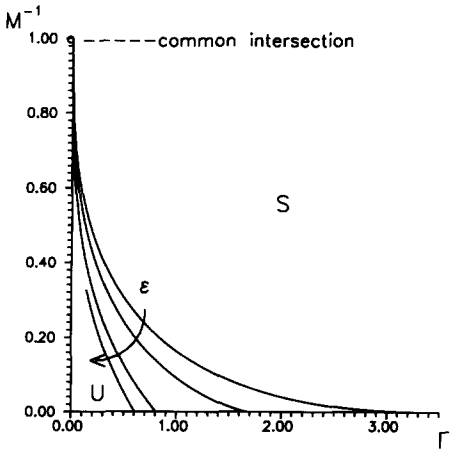

Fig. 6. Directional solidification into CSL. Plot of the critical value of M^{-1} as a function of Γ for $k = 0.3$, $S = 81.0$, $\Omega = 10.0$ and $\epsilon = \{0, 20, 40, 60\}$. The arrow indicates the direction in which ϵ increases. The interface is linearly stable (S) when the inverse morphological number is above the neutral curve. All of the curves pass through the point ($\Gamma = 0$, $M^{-1} = 1$), however the calculations for for the $\epsilon = 60$ curve were terminated before reaching that point. Notice that the range of parameter values for which the interface is stable increases with ϵ.

results from the large number of modes needed for convergence.

In the absence of flow and with k fixed, the neutral curve depends only on the surface-energy parameter Γ. In our previous figures we have used the value $\Gamma = 0.6$. In Fig. 6 we plot the critical value of M^{-1} as a function of Γ for $\epsilon = \{0, 20, 40, 60\}$. When $\epsilon > 0$ this result depends on segregation coefficient, Schmidt number, and the forcing frequency. For this figure we have again used the values $k = 0.3$, $S = 81.0$ and $\Omega = 10.0$. The nondimensional critical wavenumber approaches infinity as $\Gamma \to 0$ along these curves, and, for small values of ϵ, approaches zero as Γ is increased. Notice that the flow has a diminishing effect on stability as Γ approaches zero, and that the neutral curve always passes through $M^{-1} = 1$ when $\Gamma = 0$. In the absence of flow the system is stable for $\Gamma > 1/k$, referred to as the absolute stability limit, Γ_s. As ϵ is increased, Γ_s decreases, and for larger values of ϵ the critical wavenumber no longer approaches zero as Γ approaches the absolute stability limit.

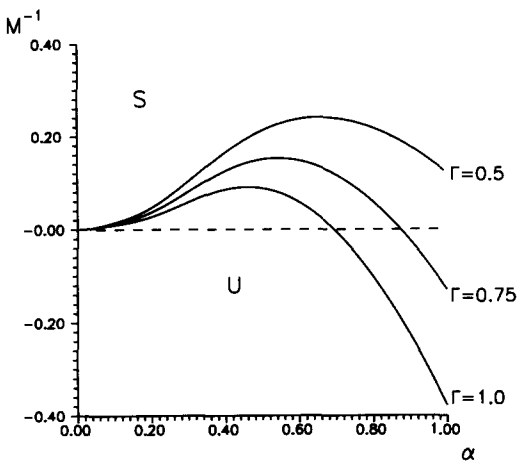

Fig. 7. Directional solidification into CSL. Plot of M^{-1} as a function of α for $k = 0.3$, $S = 81.0$, $\epsilon = 20$, $\Omega = 10.0$ and $\Gamma = \{0.5, 0.75, 1.0\}$. The region above each curve corresponds to a linearly stable (S) interface, and the region below each curve corresponds to a linearly unstable (U) interface. As Γ increases, the critical wavenumber continuously approaches zero.

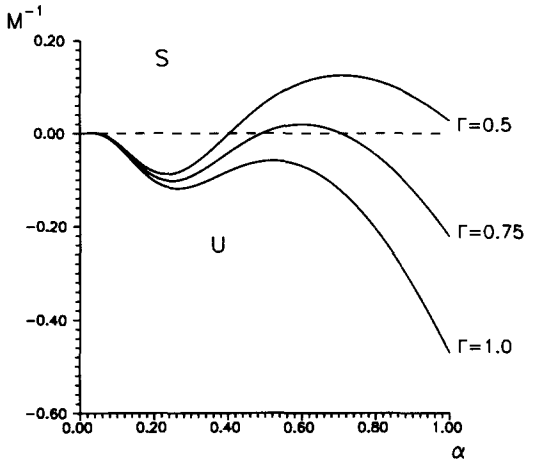

Fig. 8. Directional solidification into CSL. Plot of M^{-1} as a function of α for $k = 0.3$, $S = 81.0$, $\epsilon = 40$, $\Omega = 10.0$ and $\Gamma = \{0.5, 0.75, 1.0\}$. The region above each curve corresponds to a linearly stable (S) interface, and the region below each curve corresponds to a linearly unstable (U) interface. As Γ is increased past the absolute stability limit, the critical wavenumber abruptly shifts to zero due to the existence of two local maxima on the neutral curve.

The cases where the critical wavenumber approaches zero and where it approaches a finite value as $\Gamma \to \Gamma_s$ are further illustrated in Figs. 7 and 8. In Fig. 7 we plot M^{-1} as a function of α for $\epsilon = 20$ and $\Gamma = \{0.50, 0.75, 1.00\}$. For this value of ϵ, the critical wavenumber approaches zero continuously as Γ is increased. When Γ is increased past Γ_s, the critical wavenumber remains zero since the point at the origin of the neutral curve is fixed, but the system is absolutely stable since the morphological number must be positive. In Fig. 8 we plot similar curves for $\epsilon = 40$ and note that there are now two local maxima on the neutral curve. Tracking the location of the larger of these two maxima reveals that the critical wave number approaches a finite value as Γ approaches Γ_s. When $\Gamma > \Gamma_s$ the local maximum at $\alpha = 0$ is the larger of the two – thus there is an abrupt shift in the critical wavenumber as Γ is increased past the absolute stability limit.

In Fig. 9 we reproduce the information from Fig. 6 in terms of dimensional variables, plotting the pulling speed V as a function of the far-field concentration C_∞ with the temperature gradient

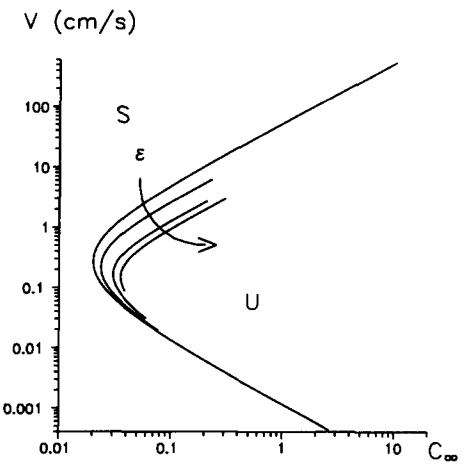

Fig. 9. Directional solidification into CSL. Plot of the neutral curve in dimensional form: V versus C_∞ for $k = 0.3$, $S = 81.0$, $\Omega = 10.0$ and $\epsilon = \{0, 20, 40, 60\}$. The arrow indicates the direction in which ϵ increases. The temperature gradient G is 200 K/cm. All of the curves extend infinitely along tangents to the portions shown. The interface is linearly stable (S) when the far field concentration is to the left of the neutral curve. Notice that the stability of the interface increases with ϵ.

Table 2
Window of stabilization, $\Omega_{min} < \Omega < \Omega_{max}$, and the approximate value of the modulation amplitude ϵ^* at the frequency Ω^* above which the instability is suppressed for *all* morphological numbers

Material	Ω_{min}	Ω_{max}	Ω^*	ϵ^*
Pb–Sn	0.7	66	10	60
Si–Sn	0	2000	5	> 500
SCN–Ace	1.5	2500	5	500

G fixed at 200 K/cm. From this figure, we see that if the far-field concentration C_∞ is sufficiently large, the interface will be unstable for a range of pulling speeds. The critical wavenumber, in units of D/V, approaches infinity along the lower branch of this curve and zero along the top branch. The stable regime lies to the left of the curve. We have previously noted that as ϵ is increased, the interface becomes more stable. This result is evident in Fig. 9; for as ϵ is increased, the nose of the neutral curve is shifted downward and to the right, and the upper branch of the curve is lowered. The lower branch of this curve is relatively unaffected, however.

To give some idea of how this scheme works in general, we present results for the three different alloys in Table 2. These three materials were chosen to represent metallic alloys (lead–tin), semiconductors (silicon–tin) and organic materials (succinonitrile–acetone). The parameter values used are those indicated previously in Table 1. The table gives the approximate range of the window of stabilization in the limit $\epsilon \to 0$ and the approximate value of the modulation amplitude ϵ^* above which the instability is eliminated by using a circular translation. Notice that ϵ^* is a function of k, S, Γ, and Ω. The angular frequency corresponding to ϵ^* is denoted as Ω^* in the table. Note that Ω^* is not necessarily the optimal frequency for stabilization purposes, although an effort was made to use a frequency close to the optimal value. We were unable to calculate a definite value of ϵ^* for the Si–Sn system. However, we were able to establish that it would be greater than 500. Calculations at larger values of ϵ require more computer memory than we had available.

In general, the interface becomes increasingly difficult to stabilize as the surface energy parameter Γ is reduced. The necessary values of ϵ and Ω needed to achieve stabilization for all morphological numbers for small Γ may not be obtainable in practice. Formulas for determining the dimensional radius r and angular frequency ω of the circular motion in terms of the nondimensional quantities and the pulling speed V are

$$r = U/\omega = \epsilon D/V\Omega, \tag{4.10a}$$

$$\omega = V^2\Omega/D. \tag{4.10b}$$

5. Other modes of instability

In all of the results we have found, the Floquet exponent σ is identically zero on the neutral curve, indicating that the frequency of the disturbance is synchronous with that of the forcing. In general, when one solves systems of differential equations having periodic coefficients, one expects that there may be a subharmonic response as well. Subharmonics are found in a number of hydrodynamic systems with time-periodic forcings that are normal to the boundary, the classic example being the problem of Faraday resonance, which leads directly to Mathieu's equation [14]. Another example of this type, involving convection and solidification in the presence of g-jitter, is discussed by Murray et al. [15]. Subharmonics are also known to appear when the temperature of the boundary in the Rayleigh–Bénard system is temporally modulated [16] or when the system is subjected to vertical oscillations [17].

We have sought subharmonic solutions to the present problem, but have not been able to locate any. It appears that this system has only synchronous modes of instability. It is interesting to note that subharmonics are also seemingly absent in the Rayleigh–Bénard system when one of the boundaries is subjected to periodic motion parallel to the boundary [18] and in modulated plane Poiseuille flow [19,20]. Thus, in the problems of which we are aware, the presence of shearing motion is correlated with an absence of subharmonic response.

6. Stability of the CSL

The stabilization of the morphological instability would be of little practical use should the system undergo a hydrodynamic instability in the same parameter regime. If we neglect disturbances to the interface shape, we have purely hydrodynamic problem for the CSL. A linear stability analysis of the CSL reveals that it is even more stable than the Stokes layer, which is believed to be linearly stable for all Reynolds numbers [21,13]. In Fig. 10 we plot the growth rate σ_r and Floquet frequency σ_i as a function of the Reynolds number with the wave number fixed at $\alpha = 0.15$ for each of these flows. Here, the Reynolds number is defined as

$$\mathrm{Re} = U\sqrt{2/\nu\omega}\,. \tag{6.1}$$

Notice that for both flows the growth rate is negative for all Reynolds numbers with the larger growth rate corresponding to the Stokes layer.

It is interesting to note that while the compression of the boundary layer has a stabilizing effect in this problem, it has the reverse effect for plane Couette flow. Plane Couette flow is also linearly stable for all Reynolds numbers. However, when suction is applied, resulting in an asymptotic suction profile (ASP), the flow becomes unstable [22] at a Reynolds number around 50000. In our previous publication [10] we pointed out that the CSL in the quasisteady limit $\Omega \to 0$ produces an effect on morphological stability that is qualitatively similar to that produced by the ASP, which is the flow generated by a steady translation of the crystal parallel to the interface. We should emphasize that this result was valid in the limit of small Reynolds number, for, in light of the information above, it appears that the situations may be very different at large Reynolds number.

No discrete eigenvalues are to be found for the Reynolds numbers lying in the gaps between these curves. There is, however, a continuous spectrum for all Reynolds numbers given by $\sigma = \sigma_r < -\alpha^2$. Thus, both the continuous and discrete spectra have negative growth rates. When the Reynolds number is below some critical value, the discrete spectrum permanently vanishes. Similar behavior

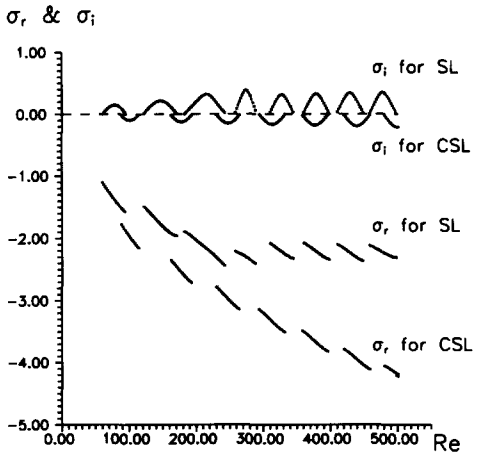

Fig. 10. Directional solidification into SL and CSL. Plots of the real and imaginary part of the Floquet exponent σ as a function of the Reynolds number with $\alpha = 0.15$ for both the Stokes layer and CSL. The real part of σ, corresponding to the growth rate, is unique and always negative for both types of flow. The CSL is always more stable than the Stokes layer. The imaginary part of σ is not uniquely determined – one may change the sign of and/or add an arbitrary integer to σ_i and still have a valid solution. For viewing convenience, σ_i for the Stokes layer is plotted with its smallest positive value, and σ_i for the CSL is plotted with its largest negative value. In addition to these discrete eigenvalues, there is a continuous spectrum for $\sigma = \sigma_r < -\alpha^2$ which is not shown.

is observed as the wavenumber is decreased. This behavior is identical to that found for the Stokes layer by Hall [13].

Eigenvalues corresponding to those of the CSL can be found for the solidification problem when the interface is disturbed, although tracking them is made somewhat difficult by their intermittent disappearance. The same continuous spectrum exists for this problem, and for large ranges of the parameter space this is the only spectrum associated with the CSL. Again both the discrete and continuous spectrum have negative growth rates, so there appears to be no hydrodynamic instability.

It should be noted that both experiments and numerical calculations show that the Stokes layer is unstable to disturbances of finite amplitude [23] at Reynolds numbers around 500. Based on Fig. 10, we anticipate that the CSL will be at least as stable as the Stokes layer when subjected to

disturbances of finite amplitude. The Reynolds number can be related to our parameter ϵ by

$$\mathrm{Re} = \epsilon\sqrt{2/\Omega S}\,. \tag{6.2}$$

For the lead–tin system which we have used as an example throughout this paper, a Reynolds number of 500 corresponds to a value of $\epsilon = 10\,000$, which places it well above the level likely to be used for stabilization purposes.

7. Conclusions

In this paper, we have shown, on the basis of linear stability theory, that nonplanar oscillations with sufficiently large amplitude may be used to suppress morphological instability during directional solidification. By choosing an appropriate frequency for the oscillations, this method may be used for a wide range of materials and operating conditions, with the principle limitation being systems with very low surface energy. It remains to be seen if the stabilized system will maintain its stability when subjected to disturbances of finite amplitude since subcritical bifurcations may be present.

Finally, we wish to point out that complete stabilization for all operating conditions is not necessary for this method to be useful. For example, although Table 2 indicates that a value $\epsilon = 500$ is necessary to stabilize a SCN–Ace interface for all morphological numbers, it turns out that a value of $\epsilon = 50$ is sufficient to extend the range of stable solute concentrations significantly.

Acknowledgements

This work was supported by grants from the National Aeronautics and Space Administration through the Graduate Student Researchers Program (TPS) and the Program on Microgravity Science and Applications (SHD). We are grateful to S.R. Coriell for bringing to our attention the work of Delves [2].

Appendix A

The constants in Eqs. (2.7) are

$$A = \sqrt{\frac{-1+\sqrt{1+16S^2\Omega^2}}{8S^2}}\,, \tag{A1a}$$

$$B = \frac{1+\sqrt{1+\frac{1}{2}\left(-1+\sqrt{1+16S^2\Omega^2}\right)}}{2S}\,. \tag{A1b}$$

The recursion relations for the coefficients in Eqs. (4.6) are given by

$$p_{nmj} = \frac{\mathrm{i}\alpha\epsilon\left(p_{n\,m-1\,j-1}P_1^{(+)} + p_{n\,m+1\,j-1}P_1^{(-)}\right)}{P_2P_3}\,, \tag{A2a}$$

$$q_{nmj} = \frac{\mathrm{i}\alpha\epsilon\left(q_{n\,m-1\,j-1}Q_1^{(+)} + q_{n\,m+1\,j-1}Q_1^{(-)}\right)}{Q_2Q_3}\,, \tag{A2b}$$

for all n, m and $j > 0$. P_k and Q_k are given by

$$P_1^{(\pm)} = \left[\alpha + (j-1)B - \mathrm{i}(n-m\pm 1)A\right]^2 - \alpha^2 - r^2, \tag{A3a}$$

$$P_2 = \left[\alpha + jB - \mathrm{i}(n-m)A\right]^2 - \alpha^2, \tag{A3b}$$

$$P_3 = S\left[\left(\alpha + jB - \mathrm{i}(n-m)A\right)^2 - \alpha^2\right] - \left(\alpha + jB - \mathrm{i}(n-m)A\right) - \mathrm{i}m\Omega, \tag{A3c}$$

$$Q_1^{(\pm)} = \left[\nu_n + (j-1)B - \mathrm{i}(n-m\pm 1)A\right]^2 - \alpha^2 - r^2, \tag{A3d}$$

$$Q_2 = \left[\nu_n + jB - \mathrm{i}(n-m)A\right]^2 - \alpha^2, \tag{A3e}$$

$$Q_3 = S\left[\left(\nu_n + jB - \mathrm{i}(n-m)A\right)^2 - \alpha^2\right] - \left(\nu_n + jB - \mathrm{i}(n-m)A\right) - \mathrm{i}m\Omega, \tag{A3f}$$

and for $j = 0$, p_{nm0} and q_{nm0} are given by

$$p_{nm0} = \delta_{nm}, \tag{A4a}$$

$$q_{nm0} = \delta_{nm}. \tag{A4b}$$

The recursion relations for the coefficients in Eqs. (4.7) are given by

$$\tilde{p}_{nmj} = \left\{\epsilon p_{nmj} + \mathrm{i}\alpha\epsilon/2\left[\tilde{p}_{n\,m-1\,j-1} + \tilde{p}_{n\,m+1\,j-1}\right]\right\} \times \left\{\left[\alpha + jB - \mathrm{i}(n-m)A + 1\right]^2 - \left[\alpha + jB - \mathrm{i}(n-m)A + 1\right] - \alpha^2 - \mathrm{i}m\Omega\right\}^{-1}, \tag{A5a}$$

$$\tilde{q}_{nmj} = \left\{ \epsilon q_{nmj} + \mathrm{i}\alpha\epsilon/2 \left[\tilde{q}_{n\ m-1\ j-1} + \tilde{q}_{n\ m+1\ j-1} \right] \right\} \times \left\{ \left[\nu_n + jB - \mathrm{i}(n-m)A + 1 \right]^2 - \left[\nu_n + jB - \mathrm{i}(n-m)A + 1 \right] - \alpha^2 - \mathrm{i}m\Omega \right\}^{-1}, \quad \text{(A5b)}$$

$$r_{nmj} = \left[\mathrm{i}\alpha\epsilon/2 (r_{n\ m-1\ j-1} + r_{n\ m+1\ j-1}) \right] \times \left\{ \left[\rho_n + jB - \mathrm{i}(n-m)A \right]^2 - \left[\rho_n + jB - \mathrm{i}(n-m)A \right] - \alpha^2 - \mathrm{i}m\Omega \right\}^{-1}, \quad \text{(A5c)}$$

for all m, n and $j > 0$. For $j = 0$ they are given by

$$\tilde{p}_{nm0} = \frac{\epsilon p_{nm0}}{\alpha - \mathrm{i}m\Omega}, \quad \text{(A6a)}$$

$$\tilde{q}_{nm0} = \frac{\epsilon q_{nm0}}{(\nu_n + 1)^2 - (\nu_n + 1) - \alpha^2 - \mathrm{i}m\Omega}, \quad \text{(A6b)}$$

$$r_{nm0} = \delta_{nm}. \quad \text{(A6c)}$$

References

[1] W.W. Mullins and R.F. Sekerka, J. Appl. Phys. 35 (1964) 444.

[2] R.T. Delves, J. Crystal Growth 8 (1971) 3.

[3] S.R. Coriell, G.B. McFadden, R.F. Boisvert and R.F. Sekerka, J. Crystal Growth 69 (1984) 15.

[4] S.A. Forth and A.A. Wheeler, J. Fluid Mech. 202 (1989) 339.

[5] A.K. Hobbs and P. Metzener, J. Crystal Growth 112 (1991) 539.

[6] K. Brattkus and S.H. Davis, J. Crystal Growth 87 (1988) 385.

[7] K. Brattkus and S.H. Davis, J. Crystal Growth 89 (1988) 423.

[8] G.B. McFadden, S.R. Coriell and J.I.D. Alexander, Commun. Pure Appl. Math. 41 (1988) 683.

[9] G.J. Merchant and S.H. Davis, J. Crystal Growth 96 (1989) 737.

[10] T.P. Schulze and S.H. Davis, J. Crystal Growth 143 (1994) 317.

[11] R.E. Kelly and H.-C. Hu, J. Fluid Mech. 249 (1993) 373.

[12] J.S. Langer, Rev. Mod. Phys. 52 (1980) 1.

[13] P. Hall, Proc. Roy. Soc. London A 359 (1978) 151.

[14] T.B. Benjamin and F. Ursell, Proc. Roy. Soc. London A 225 (1954) 505.

[15] B.T. Murray, S.R. Coriell and G.B. McFadden, J. Crystal Growth 110 (1991) 713.

[16] C.-S. Yih and C.-H. Li, J. Fluid Mech. 54 (1972) 143.

[17] P.M. Gresho and R.L. Sani, J. Fluid Mech. 40 (1970) 783.

[18] R.E. Kelly, personal communication.

[19] C.E. Grosch and H. Salwen, J. Fluid Mech. 34 (1968) 177.

[20] P. Hall, Proc. Roy. Soc. London A 344 (1975) 453.

[21] C. von Kerzcek and S.H. Davis, J. Fluid Mech. 67 (1974) 29.

[22] T.H. Hughes and W.H. Reid, J. Fluid Mech. 23 (1965) 715.

[23] R. Akhavan, R.D. Kamm and A.H. Shapiro, J. Fluid Mech. 225 (1991) 423.